



Performance improvement and start-up characteristics of a cyclorotor using multiple plasma actuators

Amine Benmoussa · José Carlos Páscoa

Received: 2 October 2020 / Accepted: 19 July 2021 / Published online: 6 August 2021
© Springer Nature B.V. 2021

Abstract In the operation of cycloidal rotors the flow structure deformation, and associated curvature, limits the possibility of achieving an optimum working point. In this study, first, we started by performing a detailed analysis of the start-up characteristics of a cycloidal rotor in order to identify the evolution of kinematic and dynamic characteristics of its operation. Afterwards, we identified the effects of applying multiple plasma boundary layer control, of dielectric barrier discharge type. This application is defined in both sides of the blades, since in cyclorotor movement they change from pressure to suction side over one blade rotation. A control law is defined to regulate the operation of the plasma actuators as the rotor blade move in azimuthal direction. The coupled multi-physics simulation of the cyclorotor and plasma flow is performed by adding to Fluent two user define functions to model the complex cyclorotor movement and the plasma momentum effect. The $k-\omega$ SST turbulence model is used in the computations. The study is performed for a cyclorotor comprised of six NACA 0016 blade profiles that rotate at 200 rpm. The results demonstrate the advantage of using multiple plasma actuators in order to control the blade flow

field. In particular, the configuration with six actuators, three in each side, was the most effective, by improving the thrust by 2.3%, as compared to the base case, and achieving a reduction in power requirements of 0.9%.

Keywords Cycloidal rotor · Start-up characteristic · Multi-DBD plasma actuators · CFD · Active flow control · Aerodynamics

1 Introduction

Nowadays, cycloidal rotor interest has been growing and showing a higher level of attention for both military and civilian applications, this rotary wing shows a great capability of producing lift, thrust and stable hover with vertical displacements in comparison with those used in helicopters.

Figure 1 presents a three-dimensional schema of a six blade cycloidal rotor device, the cyclorotor is a system in which a rotating-wing device, comprising several pitching blades, turns around an axis along the span of the blade. Such mechanical system has the capability of varying the blade pitch angle on a rotation cycle [1] with the ability to vary the direction and magnitude of the thrust vector, only by adjusting the system eccentricity, phase angle, and magnitude.

A. Benmoussa (✉) · J. C. Páscoa
Electromechanical Engineering Department, C-MAST –
Center for Mechanical and Aerospace Science and
Technologies, University of Beira Interior, Covilha,
Portugal
e-mail: amine.benmoussa@ubi.pt

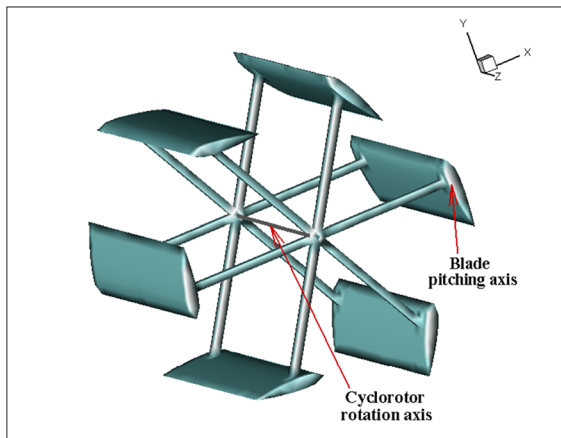


Fig. 1 Schematic of a cycloidal rotor

This important characteristic can enhance the behavior of the aircraft for diverse applications.

Several analytical models were developed for aerodynamic efficiency estimation of cyclorotor during the last two decades. McNabb [2] introduce an analytical model which included the unsteady aerodynamic theory of Garrick, for predicting the generated force and the power consumed by the cycloidal rotor. However, this feature limits its application in cases when experimental data is not available, making it strongly dependent on calibration from experimental results of the cycloidal rotor being studied. Later, using an unsteady flow formulation with a stream tube model, Benedict and Chopra [3] developed a 2D blade-element model, there study shows that it can provide rotor efficiency with sufficient accuracy.

Yun et al. [4] developed an analytical model based on momentum theory and blade element theory and presented a numerical and experimental study to verify the performance and characteristic of an unmanned aerial vehicle, they evaluated the potential of cycloidal blades for VTOL focusing on hovering and low speed forward flight. They concluded that this system can be used as powerful vector thrusting in any direction of the rotation. Monteiro et al. [5] in there study and further in [6], proposed new models for cyclorotors in a hovering state including real blade motion imposed by a four-bar linkage mechanism which allows almost instantaneous changes in the thrust direction and magnitude. They also give an idea of the camber effect intensity and its influence on rotor performance. An unsteady free wake 3D method was developed also by Tang et al. [7] to predict the

aerodynamic performance of cycloidal propellers, the results showed a reasonable agreement with the overall experimental data and the CFD results reduce the computational time and improve the computational convergence.

In recent researches, Kim et al. [8] studied the performance of a cycloidal rotor experimentally. They used NACA 0012 profile with wingspan and blade chord of 0.8 m and 0.15 m respectively. They analyzed the effect of the angle of attack of the blades, the radius of the cycloidal rotor, and the number of blades. They observed that the force generated and the power required by the cyclorotor varied proportionally with the square and cubic rotational speed, respectively. Yu et al. [9] showed in there experiments the effect of blade geometry on the performance of a cycloidal rotor. They found that the flat plate profile performed better at low Reynolds numbers. They suggested that the tapered spade did not improve performance when the trailing edge of the spade was straight. They also noted that performance improved when the maximum pitch angle at the top of the cycle was slightly lower than the maximum pitch angle at the bottom. Hwang et al. [10] analyzed the development of a cyclocopter aircraft with four cycloidal rotors of elliptical blades. they numerically and experimentally verified the viability of the cycloidal rotor as a mean of propulsion in AVMs. They conclude that the cyclogiro can produce sufficient force for the hovering state and for the low speed forward flight. In turn, Nakaie et al. [11] experimentally viewed the flow field around a cycloidal rotor using a PIV (Particle Image Velocimetry) system. The results demonstrated the presence of the downwash phenomenon around the rotor, thus providing the needed thrust. They also identified phenomena of runoff and the existence of spilled vortices in certain azimuth positions. For a better understanding of cycloidal rotors operation, Benedict et al. [12, 13] analyzed the viability of cyclorotors and the effects of various geometric parameters on a small-scale cycloidal rotor performance for powering a hover-capable vehicle. They found that a higher angle of attack of the blades allow to improve performance and increase the cyclorotor power loading. They also concluded that for low Reynolds numbers, the profile section did not play a significant role in the cycloidal rotor performance and the curved profiles reduced performance as compared to symmetrical ones.

Under the European Cycloidal Rotor Optimized for Propulsion (CROP) project, A numerical simulation was conducted by Leger and Pascoa [14], they studied the effect of harmonic vibration on a single oscillating blade and on a cycloidal rotor. They showed that using an optimal combination of harmonic vibration parameters improves the cycloidal rotor performance using amplitude, phase angle and vibration frequency. Further in [15], they studied three dimensional flow effects focusing on the secondary flow of cyclorotors in the endplat region and propeller tip. In another study, Xisto et al. [16] introduced a plasma enhanced cycloidal thruster system, they investigated the effect of plasma actuation under deep-stall conditions for a NACA0012 pitching airfoil. they implemented a single-DBD actuator placed at the leading edge and a multi-DBD configuration. They concluded that the use of multi-DBDs could delay stall and achieve faster flow reattachment than the use of a single DBD, and an optimum position arrangement of the actuators must be chosen. Later, Xisto et al. [17] performed an unsteady CFD two-dimensional analysis of the effect of several blade geometrical parameters in hovering conditions. They concluded that, for large-scale applications, the rotor efficiency and thrust capability increases with blade thickness. In the same project, Habibnia and Pascoa [18] numerically studied UAV-scale cycloidal rotor, with neural network analysis and optimization of the interaction of the downwash flow field for six vertical distances from the ground. They showed that the vertical distance of the aircraft greatly influences the efficiency of the cyclorotor in association with the pitching and rotating speed, in which the optimum operational performance is achieved by 30° and 200 rpm.

Recently, Hu and Zhang [19, 20] studied the effect of five airfoil profiles for cycloidal rotors. They found that the NACA 0015 airfoil achieved the highest figure of merit (FM), also that the maximum thickness of the airfoil significantly affected the flow field and the aerodynamic performance of the cyclorotor at the macro scale. In turn, Staško et al. [21] investigated the influence of the blade shape for a cycloidal rotor fan, they used two profiles NACA 0012 and CLARK Y to estimate the performance characteristics. They conclude that the CLARK Y profile worked more as a lift-type machine and provided higher efficiency as compared to naca 0012. Gagnon et al. [22] presented an analysis of the aeroelasticity of a cyclorotor in

forward flight; they analyzed the skin thickness and number of blades. They found that increasing the number of blades generates a greater thrust for the same power, they also showed that the flexibility and skin thickness significantly affects the pivoting rod strength and blade deformation. Furthermore, McElreath et al. [23] provided a detailed analysis of blade tip-vortex of cycloidal rotors for different aspect ratios and blade pitch kinematics. The measurements using particle image velocimetry (PIV) were conducted in water. They noticed that the strength of the tip-vortex was cyclically varied with blade azimuth position, due to the cyclic variation of the angle of attack of the blade and the dynamic virtual camber effects which leads to a periodic variation in the induced flow velocity.

In the current study, a new control actuation law considers the use of the coupled cyclorotor with multi DBD plasma actuators to control the separated flow and reduce flow losses. Active flow control in aerodynamics using DBD plasma actuators has been very effective in improving the aerodynamic performance [24] in flow scenarios involving separation and boundary layer control, this small device shows many more benefits than other flow control systems to achieve other desirable results [25], such as increase in lift, reduction in drag, reduction in noise emissions and help in reduction of airfoil stall margins. It can be used in a time of need and not in pure constant way, besides being able to fast actuation. They can work as active vortex generators [26]. Also, plasma actuators have no moving parts, being solid-state devices, which make them much simpler than equivalent mechanical devices with moving parts.

For modeling plasma actuators many different numerical models have been investigated by authors in former works, Shyy et al. [27], Massines et al. [28], Abdollahzadeh et al. [29, 30] and Suzen et al. [31]. One of the most used model is the one proposed by Shyy et al. [27, 32], where the plasma actuation is loaded as a body force into the momentum equation as a source term. The advantages of this model are simplicity, quick response, low computational cost, and good accuracy as compared with other numerical methods.

This phenomenological model is widely used by many authors to explore the application of plasma flow control, Visbal et al. [33] employed this model to explore the potential of the plasma actuator in the

control of turbulent and transitional separated flows. Orlov et al. [34] and He et al. [35] in their simulations have analyzed separation and flow control on the leading edge, over a hump, using a linear plasma distribution approach along with a lumped circuit element model. Rizzetta and Visbal [36] investigated in a numerical simulation, the effect of plasma-based flow control and total pressure loss wake reduction for a transitional highly-loaded low-pressure turbine. Recently, De Giorgi et al. [37] studied an unsteady application effect for two different configurations, micro and macro actuators on a pitching NACA 23012 airfoil with the simplified model of Shyy, operating alternately in different time periods, for pitch frequencies ranging from 20rad/s to 100rad/s to reduce unstable loads and improve stability.

Zhang et al. [38] presented the actuation strength effect, wave form, and DBD actuator frequency on flow structures induced by plasma actuator. In a study presented by Young-Chang and Shyy [39], they studied the effect of DBD plasma actuator with this simplified model on the active flow control around an airfoil of type SD7003, they studied different amplitude voltage and actuator positions for low Reynolds number and angle of attack. Riherd et al. [40] conducted a comparative study of serpentine shaped electrodes for a standard linear actuator used for flow control. They showed that the serpentine shape cause a change in the operational mechanism but does not provide an additional control of separation. Khoshkhou and Jahangirian [41] investigated the effect of multi-DBD actuators in a steady mode on the flow field of stalled NACA 0015 airfoil in a range of angles of attack 9° to 30° . They studied the effect of different locations, magnitudes and triangular-region sizes for plasma distribution on the separated flow field. Borghi et al. [42] experimentally studied the influence of DBD plasma actuators on a NACA 0015 airfoil at high angle of attack. They used a set of eight DBD actuators to generate plasma jets with different directions (vectoring effect) at different duty cycle frequencies (between 5 and 200 Hz). They concluded that the actuator placed at the leading edge presents the most effective stall recovery, and the jet's direction does not affect the stall recovery. In turn, Javadi and Hajipour [43] and Ebrahimi and Hajipour [44] have investigated numerically flow separation control on a NACA 4415 wing section in stall conditions, using arrays of discrete quasi-radial wall jets, for the wing section at

18° of angle of attack and two DBD plasma actuators with unsteady excitation on the airfoil surface to control flow separation. Akbarzadeh et al. [45] numerically investigated the impact of suction and blowing on improving the unsteady aerodynamic flow characteristics and their effect on the delay of the stall over a NACA0012 airfoil, at different angles of attack varying from 12° to 20° under low Reynolds numbers. They indicated that the vortex shedding is approximately removed when suction is applied, and the ratio of mean lift coefficient to drag coefficient increases as the suction and blowing amplitude increase. Megawanto et al. [46] found that positioning the plasma actuator at 21% chord on an isolated NACA 4415 leading edge, can decrease the drag coefficient with a percentage of 15.01% and increase lift coefficient by 17.15%.

Plasma actuators were also applied to improve the efficiency of vertical axis wind turbines. In a numerical study by Greenblatt et al. [47] they applied a plasma actuator in a pulsed actuation mode on a small vertical-axis wind turbine. They pointed out that plasma actuation was only effective on the upwind side and that the power of the wind turbine increased and the fluctuation decreased, without specifying an optimal azimuthal interval. The effect of plasma actuation on the VAWT power was also studied by Luma et al. [48]. They found that the dynamic stall's azimuth interval is around 60° or 80° , depending on tip speed ratio, and that the plasma actuation can suppress dynamic stall. The actuation can be applied optimally between 60° and 120° of the azimuth direction. Recently, Omidi and Mazaheri [49] showed that due to the use of actuators installed in a single or tandem configuration as spread between 46% and 56%, over the span length allows an energy increment up to 10.35% for the low speed ranges and 11.42% for the high speed ranges thus increasing the average output power significantly.

Due to the complexity and deformation of the flow around the cyclorotor blades, a good understanding of the aerodynamic properties and, in particular, the starting-up characteristic of cyclorotor is very important. Some researchers have focused on this issue for the VAWT performance as Worasinchai et al. [50], Biadgo et al. [51] and Zhu et al. [52]. So far, no such a study have been applied for cyclorotor systematically. In this work, first, a starting-up characteristic of cyclorotor while creating the downwash jet is

investigated. Second, multi-DBD actuators for active flow control in cyclorotor blades are studied allowing the definition of a smart control actuation law, to turn on/off the plasma actuation in different azimuth positions of its circular trajectory. This operation is tested for performance improvement.

2 Numerical modeling

2.1 Cyclorotor test-case and it’s mesh representation

For this study a two-dimensional model is used for the numerical simulation, since the main objective is limited to analyze the effect of multi-DBD actuators on a cycloidal rotor. Despite their limitations, the 2D numerical simulations can provide acceptable accuracy on predicting the aerodynamic performance of cyclorotors, as mentioned in [7, 53]. The cyclorotor domain has a circular shape with radius approximately 40 times bigger than the rotor radius (40R) and has a total number of cells of 734276 (Fig. 2), which involves three regions: environment region, rotor region and the blade region.

The environment domain is built from a fully unstructured grid that exchanges information with the rotor domain, through a sliding mesh interface, the rotor is rotating with constant angular velocity Ω . For the blades, six independent circular domains with center located at 35% of the blade chord length have been generated. The blade domain exchanges information with the rotor domain also through a sliding mesh interface, in which it is further included an area for the boundary layer to insure that y^+ is less than 1.

The blade movement and pitching is obtained in current cyclorotor applications by using a particular mechanism; the most widely adopted is the four-bar linkage shown in Fig. 3), which is imposed by the dimensions of the mechanical system. The operation of this movement depends on the control of the mechanical system, where each blade region move according to Eq. (1) and describes the blade pitch angle variation θ .

$$\theta = \frac{\pi}{2} - \sin^{-1} \left[\frac{e}{a} \cos(\Psi + \varepsilon) \right] - \cos^{-1} \left[\frac{a^2 + d^2 - L^2}{2ad} \right], \tag{1}$$

where

$$a^2 = e^2 + R^2 - 2eR \cos \left(\Psi + \varepsilon + \frac{\pi}{2} \right). \tag{2}$$

The angular pitch speed ω is defined by:

$$\omega = \frac{d\theta}{d\Psi} \Omega. \tag{3}$$

In order to get the desired pitching profile around a complete rotation, the pitching axis is located at 35% of the chord length and therefore the distance between the pitching axis and the control rod is $d = 0.120$ m. The control rod length is $L = 0.61$ m, the magnitude of the eccentricity is $e = 0.073$ m and defined as the distance from the center of rotation to the eccentricity point, the phase angle is $\varepsilon = 0^\circ$ and Ψ is the azimuth angle, the periodic pitching schedule varies from $\theta = +36^\circ$, within the top section of the rotor (90°), to $\theta = -39^\circ$ in the bottom section of the rotor (270°), resulting in asymmetric pitching profile.

2.2 DBD plasma actuator model

One of the most famous models from the phenomenological modeling approach is the one proposed by Shyy et al. [27]. This model offers a good trade-off between accuracy and simplicity as compared with other models. As was presented by Abdelraouf et al. [54] in their work. They simulated the effect of the plasma actuator on a NACA 0012 airfoil with Shyy and Suzen models to check the accuracy of each model. They reported that the Shyy model is reasonable accurate to be used for the simulation of the plasma effect, with the assumption of the linearity of the electric field, giving almost accurate results as Suzen model, and less amount of time and iterations to attain converged solution than the Suzen model. This phenomenological model was also approved by many authors for unsteady simulation in recent papers among them; Lu Ma et al. [48], De Giorgi et al. [37] and recently Yu Haocheng and Zheng Jianguo [55].

Therefore, the simulation conducted here with the Shyy model allows an analysis of the DBD effects with a significant accurate model in a reasonable time,

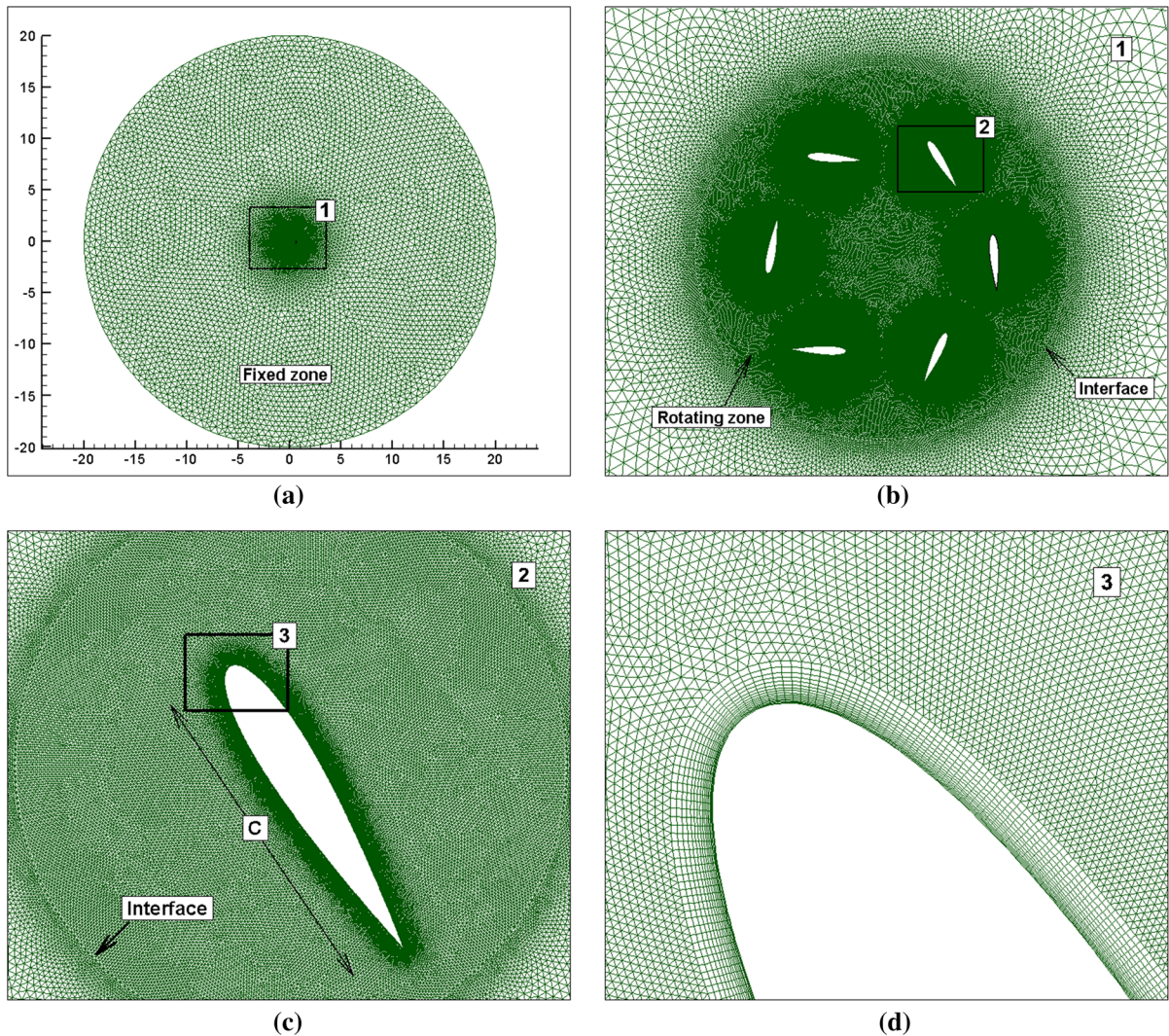


Fig. 2 Computational grid domain: **a** global view of the mesh; **b** rotor domain; **c** blade domain; **d** detail view of a blade

considering the small time-step and the number of computations needed for the parametric study.

In this model, the body force field generated by the actuator was approximated using a linear expression, as a triangular force distribution near the exposed electrode side with the dimensions of a and b as shown in Fig. 4. The electric field is strongest in the region near the electrodes and decreases in strength further away from the electrodes.

The electric field strength \vec{E} is linearly distributed in OAB and obtained as,

$$|\vec{E}| = E_0 - C_1x - C_2y, \tag{4}$$

where E_0 is the value of the field at the origin of the local coordinate axis approximated as,

$$E_0 = \frac{U_0}{d}, \tag{5}$$

and (x, y) refer to the actuator local coordinate system, d is the distance between the two electrodes in the x direction. C_1, C_2 are parameters adjusted to allow the breakdown voltage at the border with the minimum electric field strength [27] computed from,

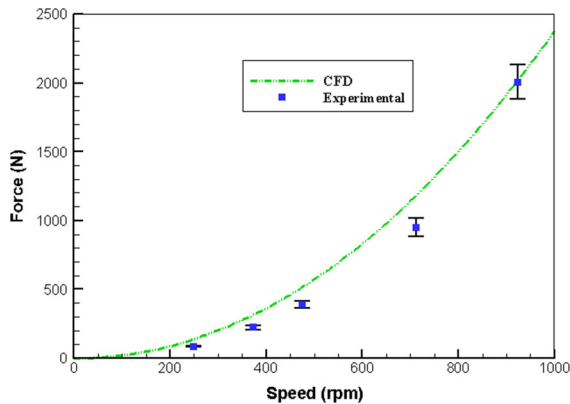


Fig. 6 Comparison of cycloidal rotor thrust as a function of rotational speed obtained from our CFD model and from experiments, [59]

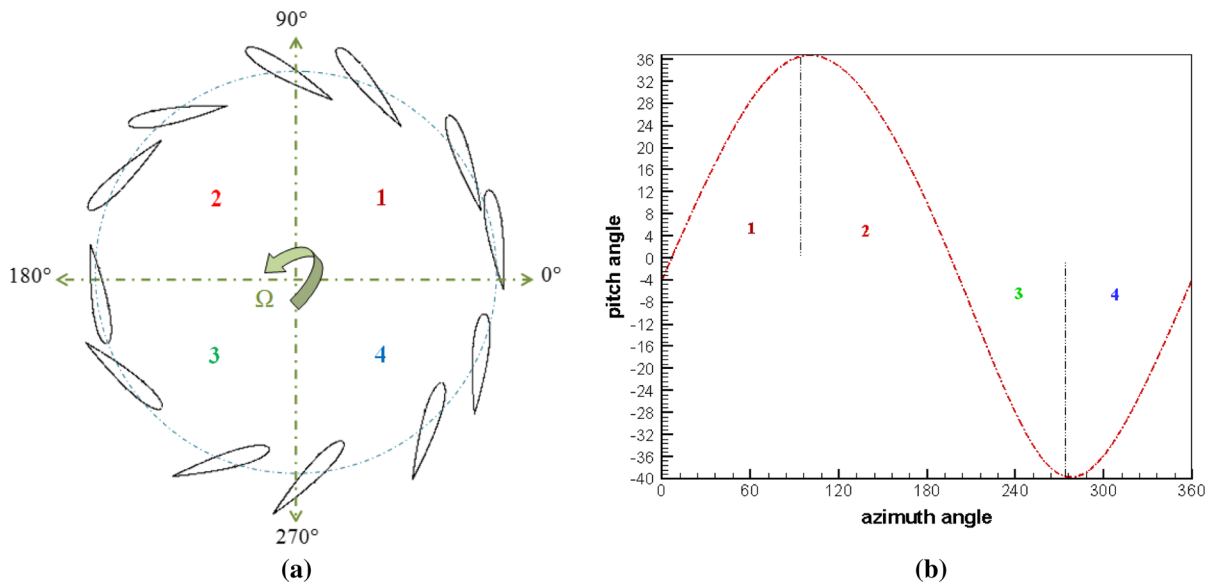


Fig. 7 Sinusoidal low pitch system: **a** blade positions at different azimuth angle; **b** pitch angle variation as function of azimuth angle

in 2D, the blades and rotor movements and also the body force of the DBD plasma model are coded, implemented into the user defined functions (UDF) and loaded into the Fluent solver. The Gauss–Seidel iteration method is used to solve the discrete equations with a pressure-velocity coupled algorithm and a fully-implicit second-order time discretization method, while, for space interpolation, a second order linear-upwind scheme is adopted.

Due to the complex mechanism of blade rotating and pitching oscillations in cyclorotors and the flow structure deformation and associated curvature, besides the relatively large computational domain. Turbulence models such as Large Eddy Simulation (LES) or Direct Numerical Simulation (DNS) would result in extremely high computational costs, that must be avoided. Therefore, The selected turbulence model for the current study is the $k-\omega$ SST. This model gains the advantage of a two-equation eddy-viscosity turbulence approach, where the free stream can be resolved by $k-\varepsilon$ and the shear layer regions are treated with the $k-\omega$ model.

As it was illustrated by many authors, namely, Tang et al. [53], Jakson et al. [15], Abdollahzadeh et al. [30], Bennoussa and Páscoa [56], among others, the 2D-

RANS with $k-\omega$ SST, transition is capable of capturing the main flow features and provides acceptable results and a satisfactory agreement with the experimental results. Furthermore, the model used in the current simulation was also considered adequate in terms of computation costs and accuracy by Habibnia and Páscoa [18], Singh and Páscoa [57] and Rezaeiha et al. [58].

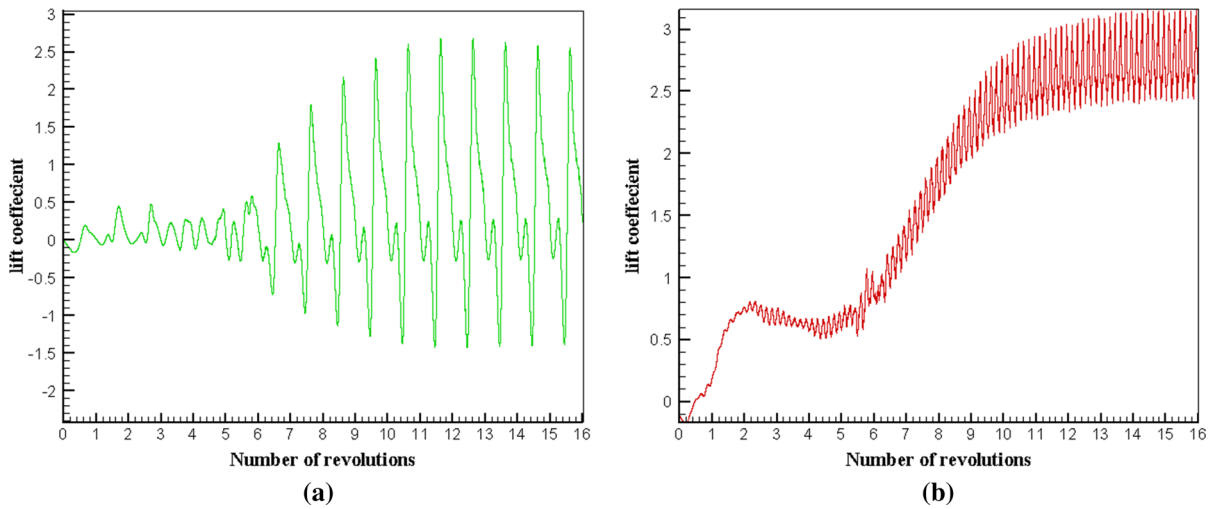


Fig. 8 Variation of the lift coefficient as function of number of revolution: **a** lift coefficient for a blade; **b** total lift coefficient

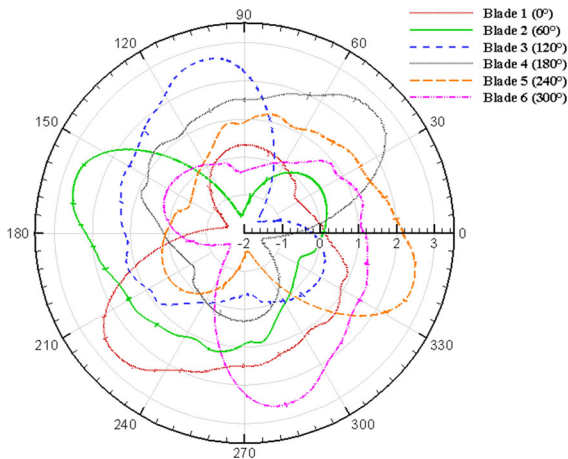


Fig. 9 Lift coefficient for the cyclorotor blades as a function of the azimuth position for one revolution

The boundary condition has been defined as non-slip in the walls and all variables are extrapolated at the outlet. The convergence criterion is that the residuals of all variables are less than 10^{-5} . The time step size is used to obtain a rotor rotation of 0.1° per time-step.

3 Results and discussion

3.1 Isolated cyclorotor

The flow behavior induced by cycloidal rotors experiences many curvatures and deformations while creating the downwash jet. In order to obtain a better state of operation, different investigations are indispensable, a detailed understanding of the flow mechanism is thus necessary to achieve higher performance.

3.1.1 Grid sensitivity analysis

In order to verify the grid independence, three distinct meshes were considered with a different number of cells, namely 590102, 734276 and 810216. Figure 5 presents the comparison of the predicted dimensionless time ($t^* = t.U/c$) histories of lift coefficients on the cycloidal rotor blade for three sets of grids. As it is observable, after the cyclorotor attaining stability it undergoes a periodic oscillation on the lift coefficient. It can be seen that the difference between the lift coefficient on the fine and medium meshes becomes negligible. Therefore, we performed our simulation using the medium mesh. The grid has a total number of 734276 cells in the entire computational domain and 89263 cells in each blade domain.

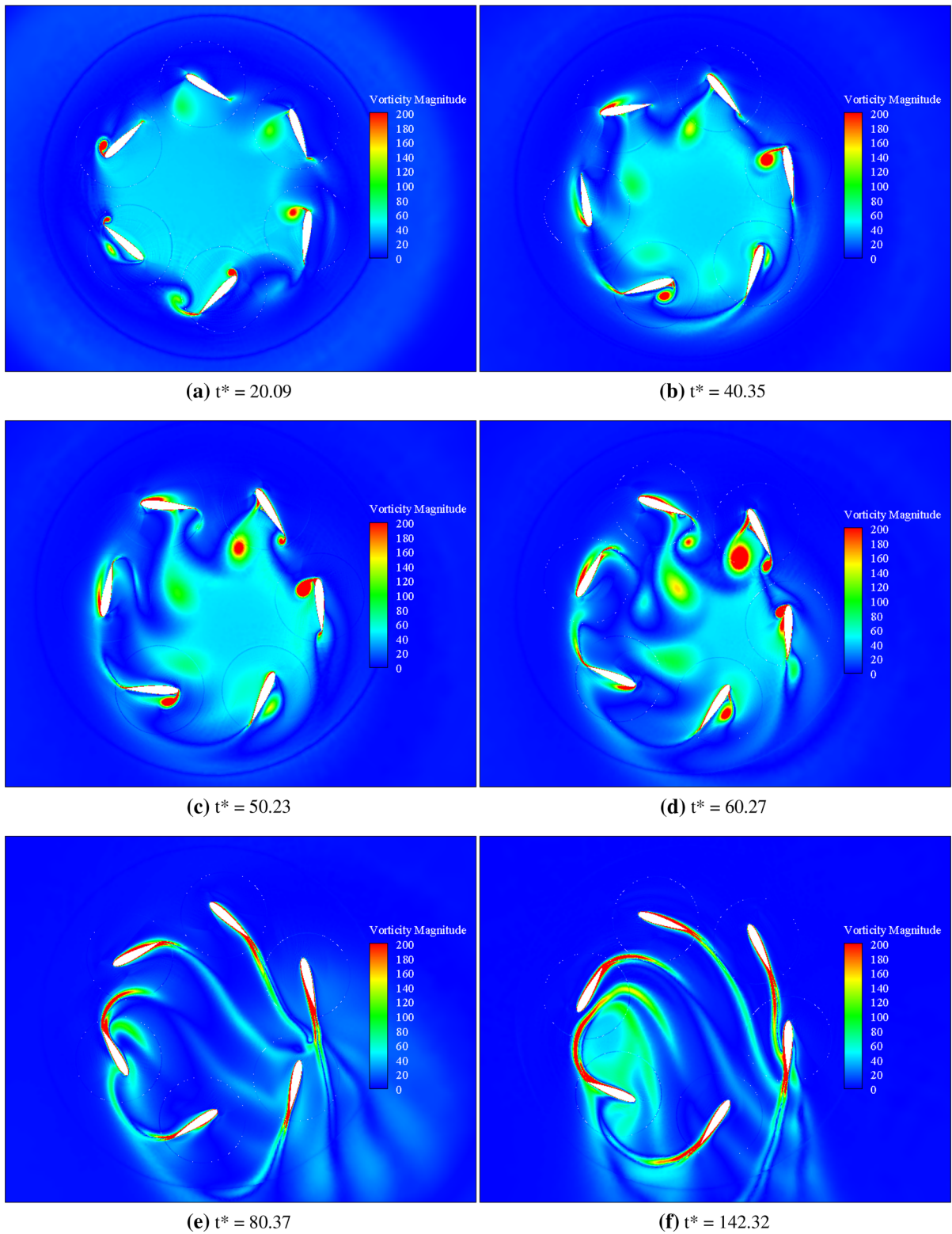


Fig. 10 Instantaneous vorticity contour around the cyclorotor blades at different dimensionless time (t^*)

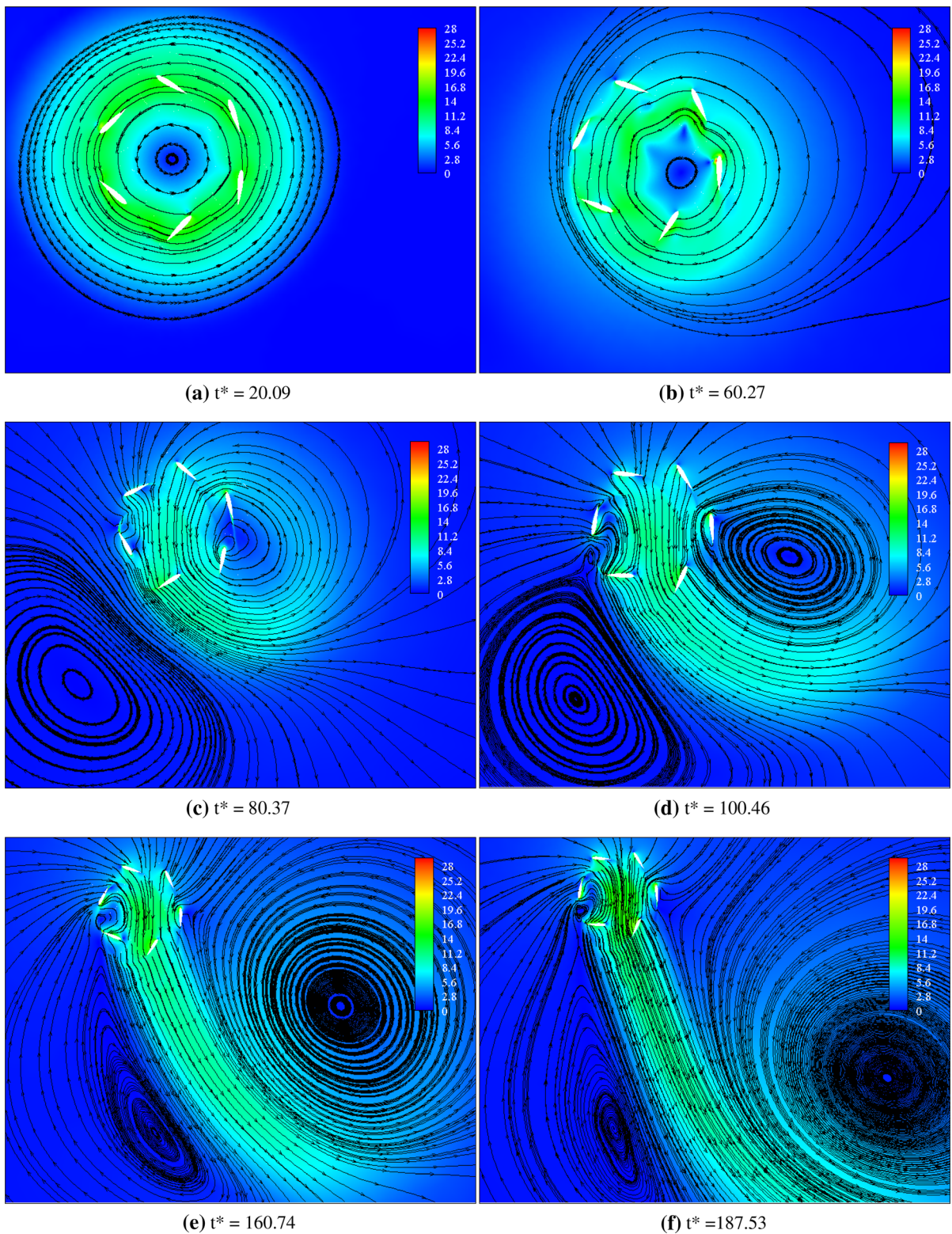


Fig. 11 Instantaneous velocity magnitude contour and streamlines around the cyclorotor blades at different dimensionless time (t^*)

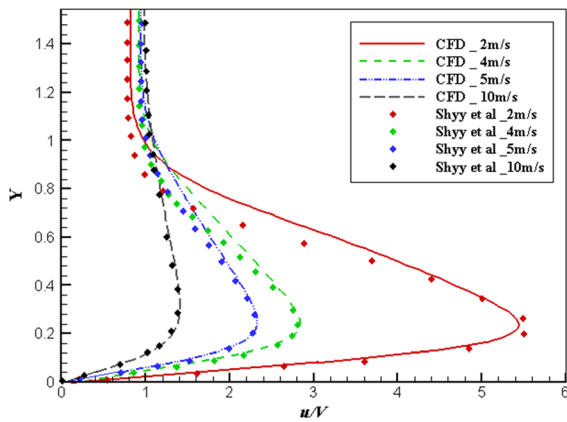


Fig. 12 Velocity profiles for different free stream velocities at the same position (ST4) obtained from our CFD model and from [27]

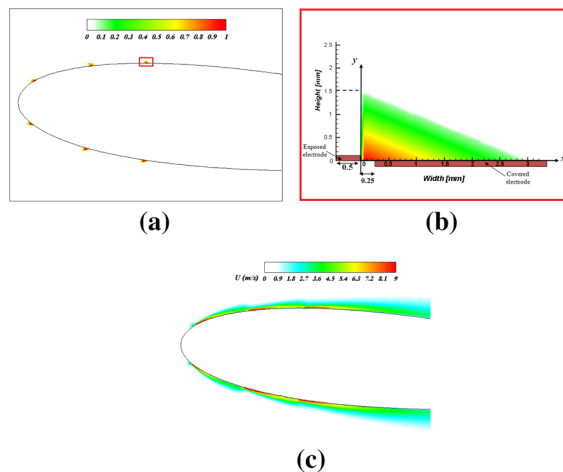


Fig. 13 **a** Multi-DBD actuators positions on a cyclorotor blade located at 120°; **b** Electric field distribution showing the DBD acting zone; **c** Induced flow computed with multi-DBD actuators on cyclorotor blade

3.1.2 Base case validation

The validation procedure of the computational model for the cyclorotor has been done against the experimental results (Wills and Schwaiger 2012) [59]. The IAT21-L3 configuration uses six NACA 0016 blades, with chord to radius ratio of 0.5, a span to diameter ratio of 1, the pitching axis is located at 35% of the chord length, and the distance between the pitching axis and the control rod is $d = 0.120$ m. The control rod length is $L = 0.61$ m, the magnitude of the eccentricity

is $e = 0.073$ m, and is defined as the distance from the center of rotation to the eccentricity point, the phase angle is $\varepsilon = 0^\circ$ and Ψ is the azimuth angle, the periodic pitching schedule varies from $\theta = +36^\circ$ in the top section of the rotor (90°), to $\theta = -39^\circ$ in the bottom section of the rotor (270°), both defined in order to obtain the desired pitching profile.

As shown in Fig. 6, the results show a good agreement with the experimental data of the IAT21 rotor considering the complexity of the flow in this cyclorotor.

Figure 7 shows the pitch angle variation as function of azimuth angle for a blade from our CFD result in the pitching law system according to Eq. (1), where the variation of the pitch angle is identical to the sine curve.

The blades of the cyclorotor describe a cycloidal path, in the upper half in region 1 between 0° and 90° , the blade introduces an up-stroke towards the maximum external angle of attack, after 90° in region 2, the blade acts with a down-stroke by resuming to its original angle of attack. In the lower half between 180° and 270° , in this third region the blade introduces an up-stroke to reach it’s maximum internal angle of attack before it comes back for the internal down-stroke again in region 4. It can be seen also from Fig. 7 that with this mechanism, the pitching extremes does not occur exactly at 90° and 270° , but with a small phase delay.

3.1.3 Aerodynamic force

Figure 8 shows the relation between the lift coefficient and number of revolutions (flow time). It can be seen that the evolution of the lift coefficient for both graphs in Fig. 8a, b, can be divided in two phases, instability phase and stable periodic oscillation phase.

The instability is due to the cyclorotor adjusting its configuration to forces incurred by the flow on the variable pitching blade that changes its orientation and angle of attack to generate optimal lift force. Therefore, it is sensitive to the variable angle of attack of each blade at the initial stage, to struggle, while producing lift force for a complete revolution. As the blades rotate further, and after 10 revolutions, the cyclorotor gains stability under a periodic oscillation for the lift coefficient.

Figure 9 shows polar curves of lift coefficient for the cyclorotor blades as a function of the azimuth

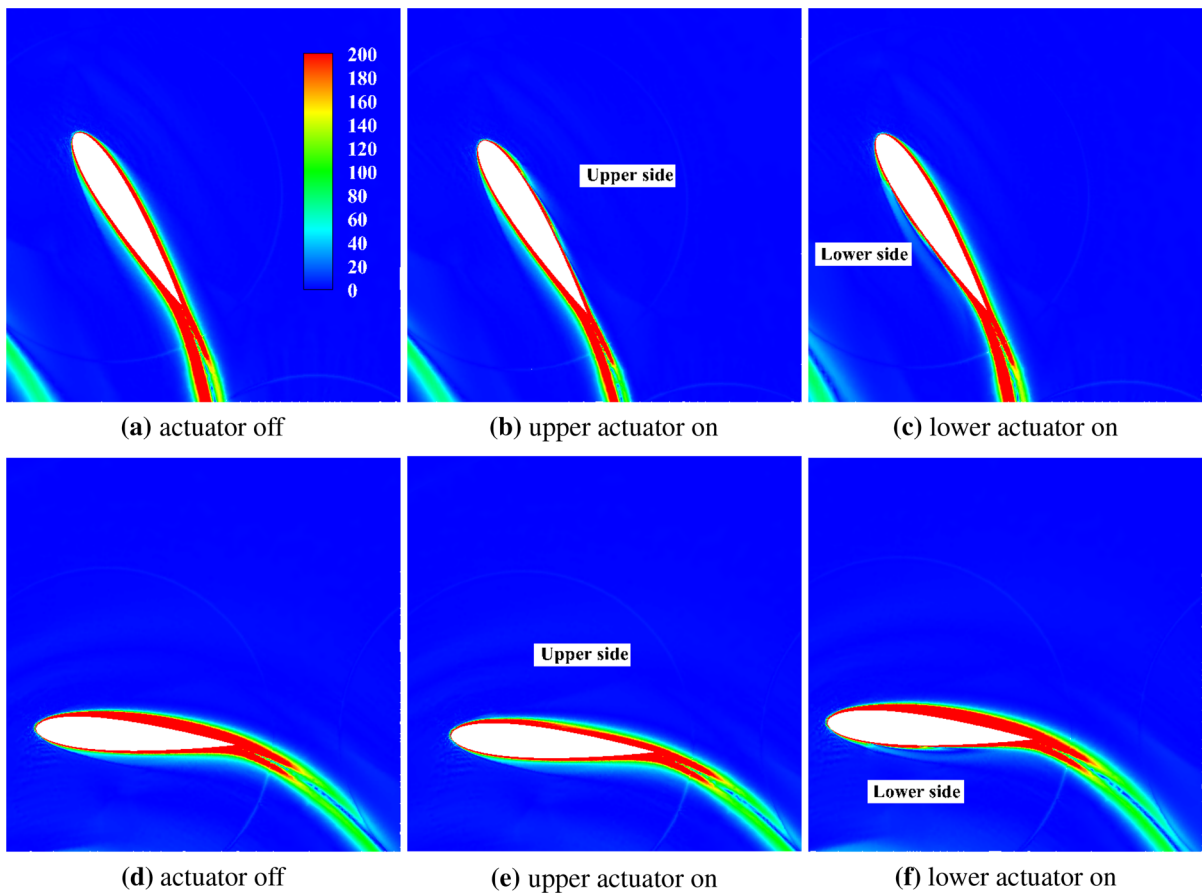


Fig. 14 Vorticity magnitude comparison of a blade operate in upper half at ($\Psi = 60^\circ$) and ($\Psi = 120^\circ$)

position for a complete cycle. For the first blade located at 0° in the upper half, between 0° and 60° there is a small decrease and increase in lift because of the slight change from the negative to positive angle of attack, then the blade produces negative lift and reaches its minimum at 160° , it starts increasing afterwards and produces a positive lift between 180° and 360° (lower half) and reaches its maximum at 220° after which it starts decreasing as the angle of attack decreases. Further more, in the upper part, the blade has a negative camber and therefore a smaller lift is generated as compared with the lower half, where the blade has positive camber. This is due to the pitch angle of each blade which is changed cyclically by mechanical means [8]. In that way, the blades find positive angles of attack at the top and at the bottom of the azimuth position and generate upward force, but at the left and the right positions there is a smaller force,

because the blade has a low angle of attack. A similar behavior is noticed for the other blades with a phase difference corresponding to a maximum lift coefficient of 60° of azimuth angle.

3.1.4 Vorticity Field

Figure 10 presents the instantaneous vorticity contours around the cyclorotor blades at different dimensionless time ($t^* = t.U/c$), six typical times are considered. From Fig. 10a, it can be seen that there is a strong formation of a leading edge vortex from the upper side of the blade, when the blade is operating in the upper half zone. On the other hand, when the blade is operating in the lower half of its circular trajectory, where the blade is pitched in the opposite direction, the formation of a leading edge vortex is started from the lower section of the blade. This is due to the dynamic

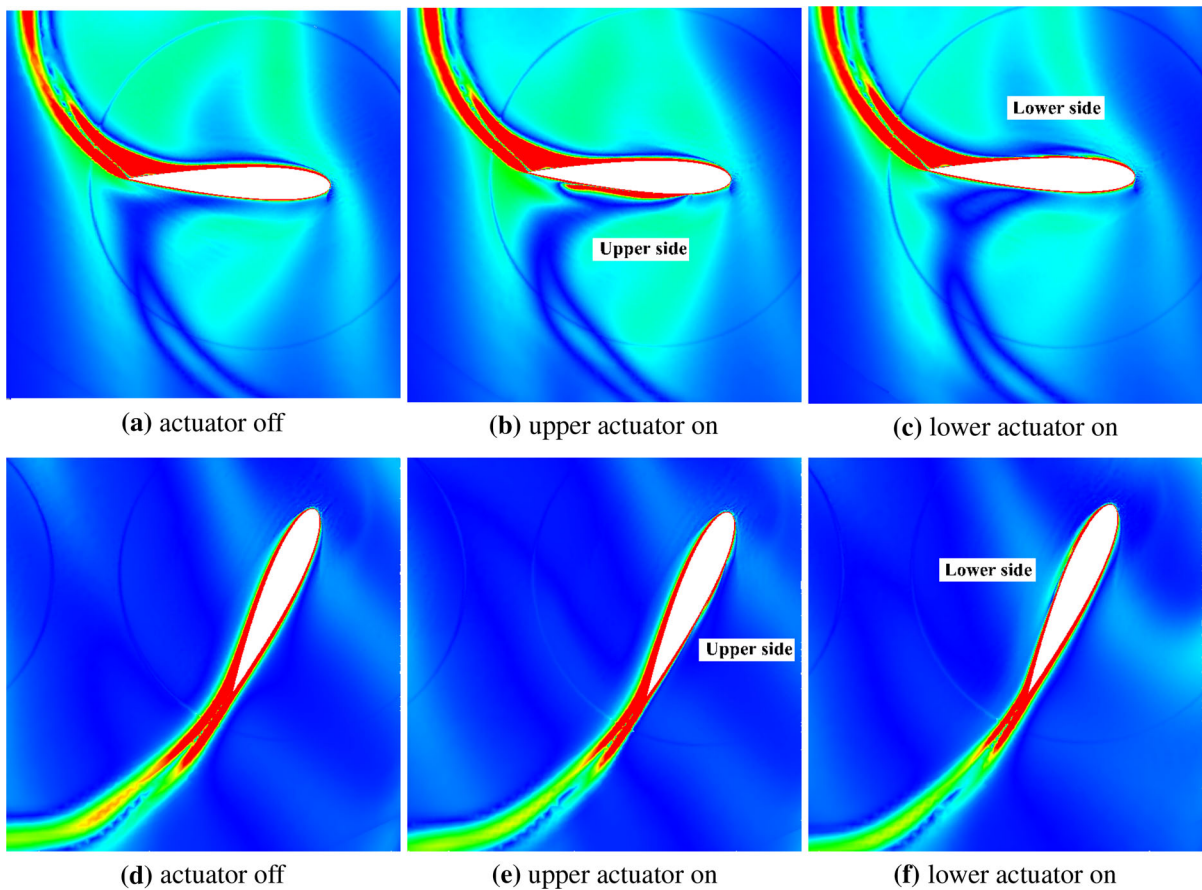


Fig. 15 Vorticity magnitude comparison of a blade operate in lower half at ($\Psi = 240^\circ$) and ($\Psi = 300^\circ$)

virtual camber which results in a negative camber equivalent at the top position, and a positive camber equivalent at the bottom position, in which this reversal of the virtual blade camber from upper to lower half results in a completely different dynamic stall processes in the upper and lower zones of the circular trajectory of the cyclorotor.

As the angle of attack of the blades increases as shown in Fig. 10c, d, the size of the vortex increased and begins to separate from the leading edge, and the flow in the central region of blades is extremely separated also at the inner rotation domain, during this phase, the flow separation is much stronger than before, since the blades face a deep dynamic stall. Also the vorticity develops with the rotation of the blades and start moving to the trailing edge.

When the blades rotate further in Fig. 10e, f, the separated vortex remains flattened and interact with the blades which reduce the instantaneous angle of attack, also a strong wake effect is remarked on the trailing edge of the blades which affect the up coming blades.

During the entire rotation, a periodic shedding of a vortex was found with flow attachment on the airfoil surface, flow separation from the leading edge then to the trailing edge and flow reattachment to the airfoil surface. Further, we can notice that in the upper half area the vortices on the upper section of the blade are more developed, when the blade rotates further in the lower half, the vortices are now generated on the bottom surface of the blade (Fig. 10f).

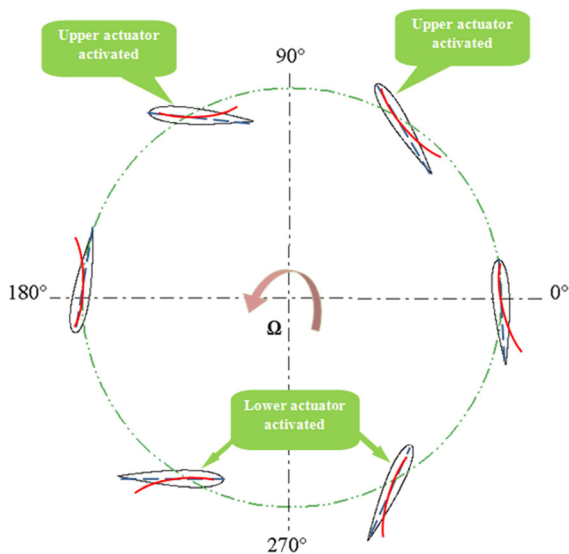


Fig. 16 Virtual chord-line due to virtual camber effect on the cyclorotor blades showing the places where the DBD is activated at different azimuth locations

3.1.5 Velocity contour

Figure 11 presents the instantaneous velocity contours and streamlines around the cyclorotor blades at different dimensionless time ($t^* = t.U/c$), six typical times are considered. In Fig. 11a inside the rotor cage, a recirculation zone is visible, whose streamlines are closed and symmetrical with respect to the cyclorotor rotation in counter clockwise direction. As the blades rotate further in 11b this zone moves with an

inclination towards the right, before the flow starts entering and coming out from the rotor cage which produces a small downwash inclined towards the right, and the vertical component of the flow velocity is highly influenced by the preceding blade, while two circular vortex zones are created on the left and right sides of the cyclorotor as shown in Fig. 11c.

Due to rotation and the different velocities at the top and bottom positions, caused by the cyclorotor and the interactions of blades wakes, the downwash jet becomes stronger and the inclination angle of the downwash flow is decreased with an associated change in pattern and size of the two vortex zones, which can be clearly seen from Fig. 11d, e.

In Fig. 11f it is clearly shown that the incoming flow descends directly inside the rotor cage without any circulation. In this period the flow is passing by three stages: first, inhaling region where the flow comes from the majority of the upper half zone of the cyclorotor; second, the downward flow inside the rotor cage, where the incoming flow entered to the inside cage of the cyclorotor and moves downward; third, a downwash jet flow is generated while exiting the bottom zone of the cyclorotor, here the outflow is inclined with a small rightward angle with respect to the perpendicular, with a strong downwash caused by the cyclorotor and the interactions of blades wakes as compared to the previous times, and it results in a deflection of resultant thrust.

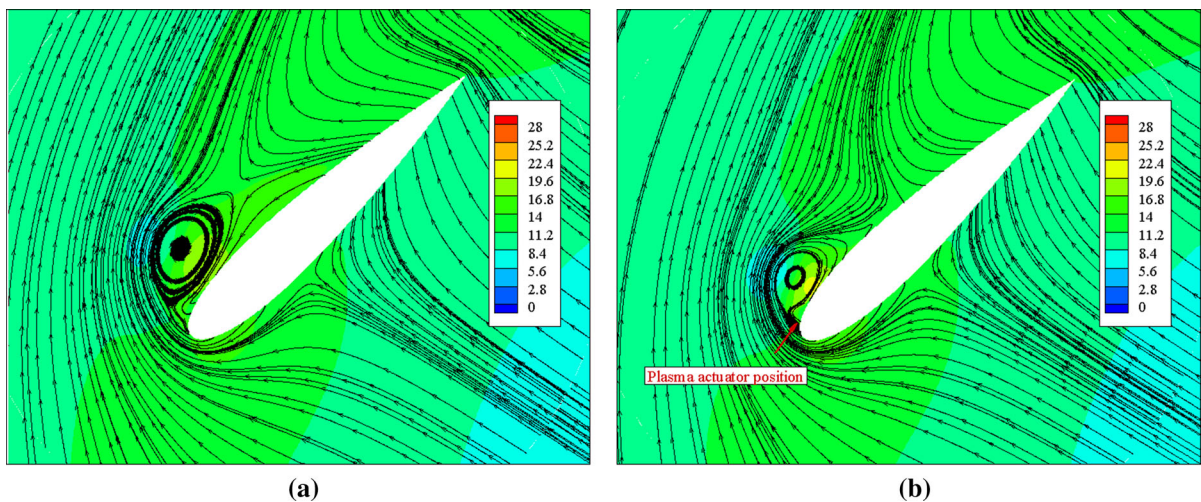


Fig. 17 Velocity contours and relative streamlines comparison around a blade at 150°: **a** actuation off; **b** upper actuator activated

3.2 Coupled cyclorotor with plasma actuators

3.2.1 DBD model validation

First, to validate our numerical model, we used a numerical simulation of Shyy et al. [27] on a 0.0205m flat plate. The computational domain is a 2D rectangle on x-y plane with a plasma actuator placed at the bottom of domain in the solid wall. The different parameters used to define this DBD are the elementary charge $e = 1.602 \times 10^{-19}$, the charge density $\rho_c = 1 \times 10^{17} \text{ m}^3$, the applied voltage frequency of 3 kHz, the applied voltage of 4 kV rms, the breakdown electric field strength 30 kV/cm and the discharge time $67 \mu\text{s}$.

Figure 12 presents a comparison of the normalized velocity profiles at the same position (ST4) for various free stream velocities 2,4,5 and 10m/s of our CFD results with Shyy et al. [27]. The comparison of the results shows a good agreement for each of the applied free stream velocities.

The multi DBDs are located on both sides on each cyclorotor blade and the first plasma actuation generated by the first actuator is located at 2% from the leading edge of the airfoil (Fig. 13a), Fig. 13b shows the modeled triangular force distribution with height $a = 1.5 \text{ mm}$ and width $b = 3 \text{ mm}$. Figure 13c presents the velocity induced by the multi-DBD plasma actuators on the cyclorotor blade. It can be seen the jet formation along both sides of the blade due to the plasma actuation where the body force is generated from the

exposed electrode to the covered electrode direction, also the benefic of using multi-DBD configuration which could increase the momentum of resulting jet then drives the fluid along the airfoil surfaces.

3.2.2 Effect of first pair of actuators

In cycloidal rotor, despite the fact that the blade's geometric angle of attack is identical with respect to the tangent of trajectory, the incident angles of attack may be different along chord line. Thus the cases of the upper top position and the lower one do not have same aerodynamic characteristics, due to rotating velocity and the effective variation of the angle of attack along the chord so each point at chord line has different rotating velocity. As if the blade at upper position has negative camber and the blade at lower position has positive camber which can introduce significant changes in the aerodynamic behavior of each blade and as consequence, a smaller force is generated on top half as compared with the bottom half, this is the virtual camber effect.

To cancel the virtual camber effect on cyclorotors, one solution could be the use of geometrical cambered blades [17] in the rotor, which can improve rotor performance if the camber can be changed to the other direction in the upper and lower half of the rotating cycle.

Active flow control techniques such Dielectric Barrier Discharge (DBDs) plasma actuators can reduce, or avoid flow separation which can change

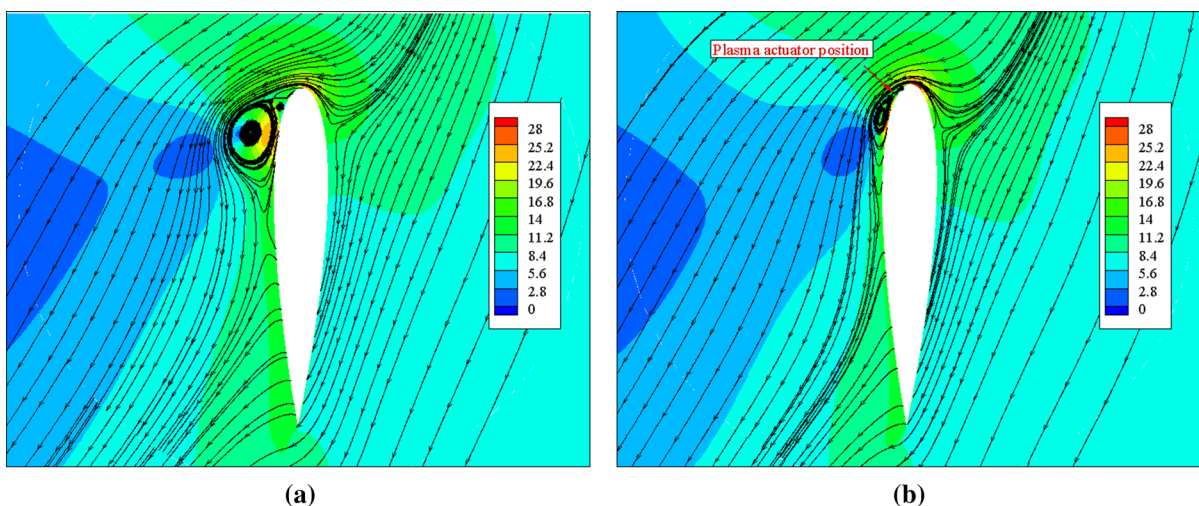


Fig. 18 Velocity contours and relative streamlines comparison around a blade at 350° : **a** actuation off; **b** lower actuator activated

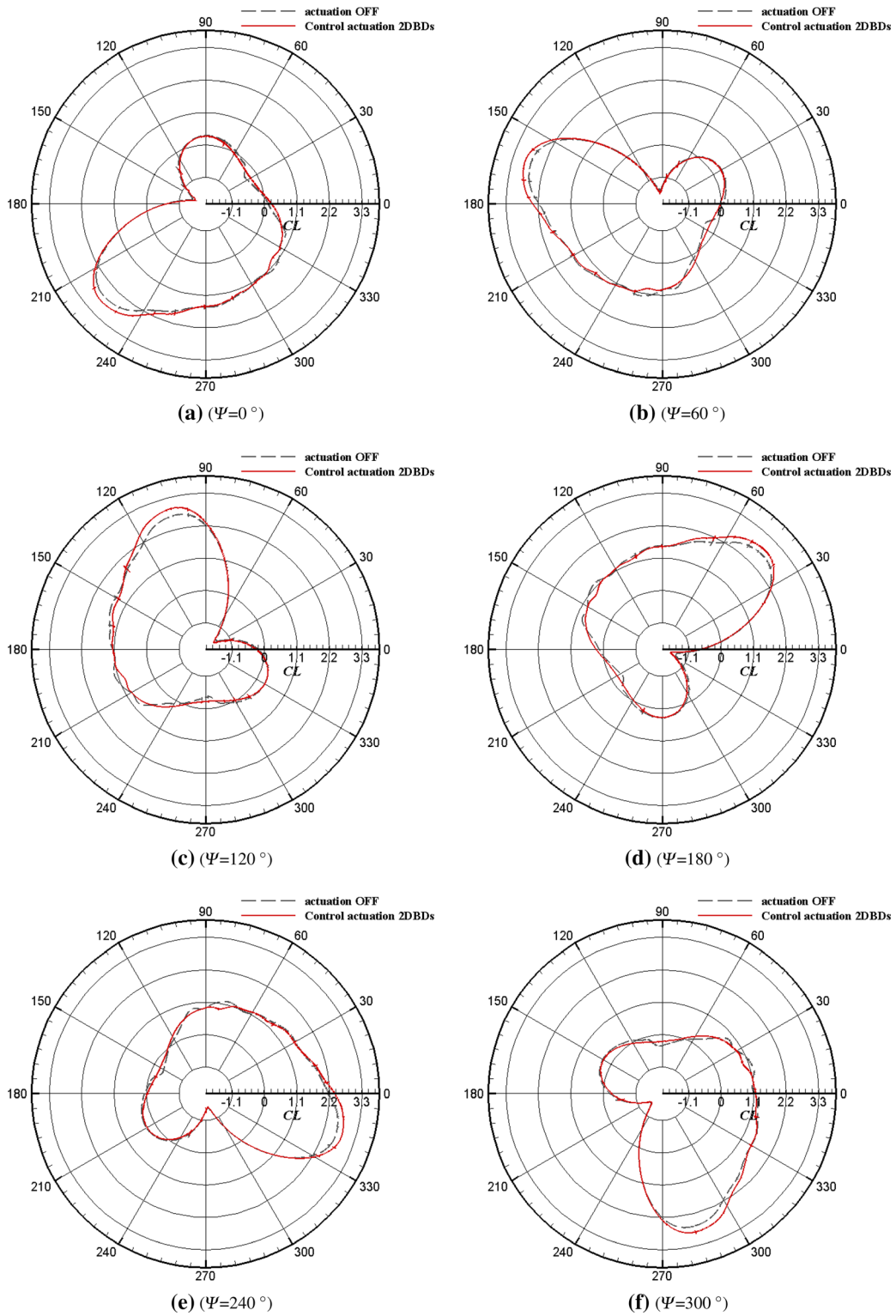


Fig. 19 Lift coefficient comparison for the base case and the control actuation with 2 DBDs

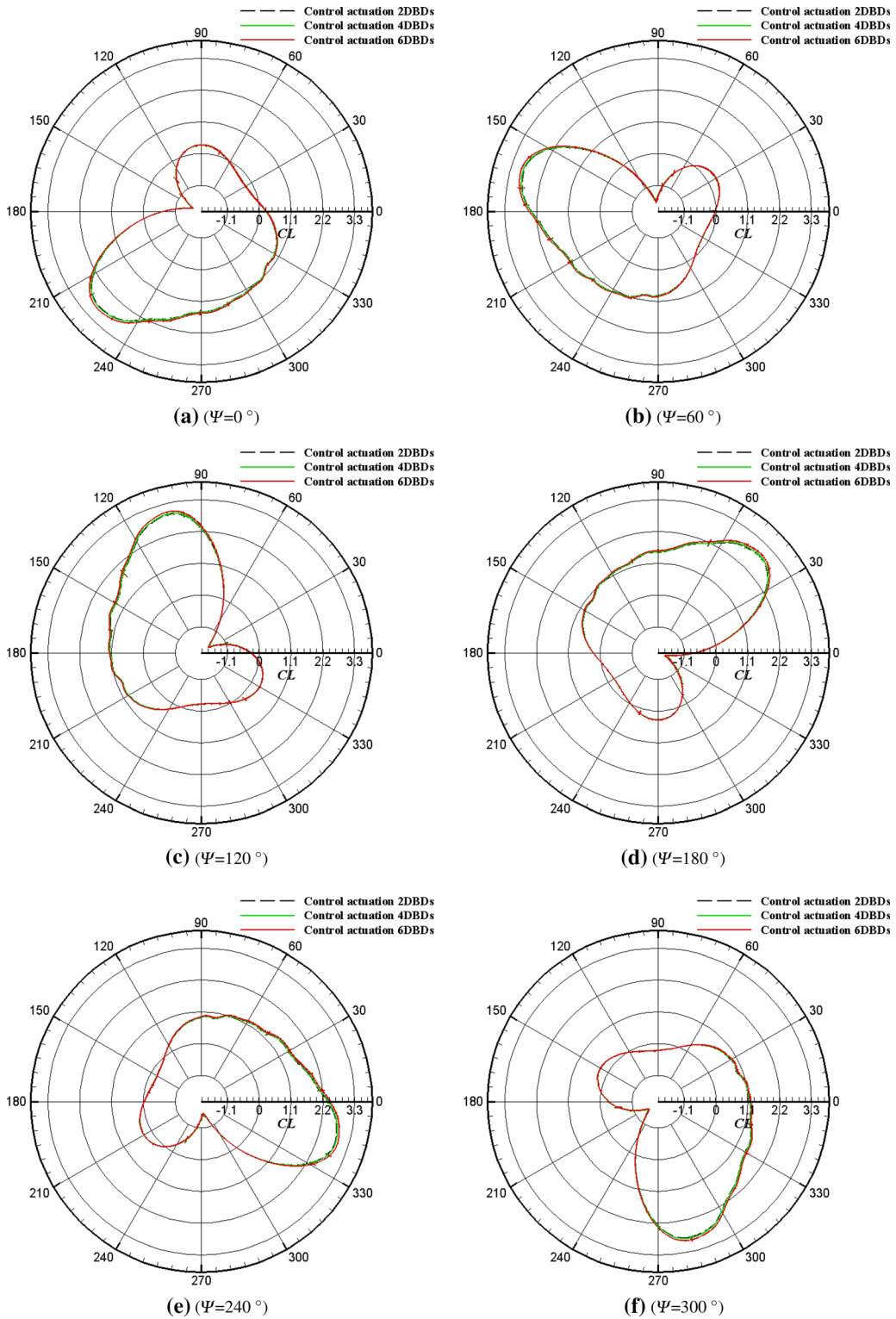


Fig. 20 Lift coefficient comparison for the control actuation with two, four and six-DBDs

the flow field around the blades, and contribute to reduce the effect of the virtual camber on the cyclorotor by generating a counter-virtual camber on the airfoil.

As a matter of fact, in Fig. 14, we show the effect of DBD plasma actuators on vorticity field where the blade operate in upper half zone, at 60° where the blade introduce an external upstroke and 120° where the blade introduce an external down-stroke, it is obvious that the upper actuator reduce the vorticity which tends to flatten on the blade surface and is then diminished. On the other hand, the lower actuator seems not to reduce the vorticity due to it is developed on the upper surface of the blade. Figure 15 shows the effect of plasma actuators on vorticity field where the blade located at 240° which introduces an internal upstroke and 300° which the blade introduces internal down-stroke. The opposite of what is the case in upper half, the lower actuator located on the lower side of the blade is more efficient as compared the upper one, which reduce the strength and size of the vorticity as shown in Fig. 15c, f, therefore causing a change in the operation of the cycloidal rotor and thus a change in the force produced. For this purpose, a control law is used to activate the upper plasma actuator in the upper half and the lower one in the lower half of the cycloidal patch as shown in Fig. 16.

Figure 17 shows a comparison of relative streamlines around a blade located at 150° with actuation off and upper actuator activated. Due to the leading edge vortex, a separation and re-circulation zone is appeared on the upper surface of the blade. When the upper actuator is activated, the body force field creates an induced flow near the airfoil surface, so the separation length is small and the size of the re-circulation zone is reduced as compared to the base case. Further, Fig. 18 presents the relative streamlines comparison for actuation off and lower actuator activated around a blade located at 350° of azimuth angle. Here the separation and re-circulation zone is on the lower surface of the blade, and similar effect is noticed for the lower actuator where the flow is attached to the blade and a significant reduction of the re-circulation zone can be seen as compared to the base case, but does not eliminate the separation completely. These changes are expected to be advantageous for the lift coefficients.

The lift coefficient comparison for the base case and the control law for the blades is shown in Fig. 19

using the first pair actuators located on the leading edge of the blades (as shown before in Figs. 17, 18). It is clear that in each blade, the maximum lift coefficient is increased when using the control law as compared to the base case, depending on the position of each blade where the upper actuator is activated in the upper half and the lower one in the lower half but also we notice that between 300° to 350° and 30° to 70° and also between 120° to 160° there is a slight decrease in lift coefficient as compared to the base case because there is a time delay when the upper actuator is turned off while the lower actuation is turned on/off.

3.2.3 Effect of multi-DBD actuators

To compare the use of multi-DBD actuators, we activate four DBD actuators, then six DBD actuators with the same control law as used with the first pair actuator, the results are shown in Fig. 20. It can be seen that using 4 actuators produced almost the same lift as 2 actuators, when using 6 actuators, it produce more lift as compared with the previous cases, this is explained by using 6 DBD actuators more momentum is being applied to the flow in which more velocity is produced by the actuators in a larger section on the blade surface.

In Fig. 21, the velocity magnitude contours comparison between base case and the cyclorotor coupled with six plasma actuators is presented showing the exit flow direction and magnitude. It can be seen that using six-DBD actuators can change the flow field around the cyclorotor blades which it is showing a higher exit flow as compared with base case, therefore causing a change in the operation of the cyclorotor and the force generated.

The aerodynamic analysis requires an estimation of the forces generated by the cyclorotor and the power requirement, two parameters are considered for the operating mechanism: power loading (PL) which corresponds to the net thrust over the net power, and disk loading (DL) which corresponds to the produced thrust over the disk area, which are defined as follows.

$$PL = \frac{T_n}{P_n}, \tag{12}$$

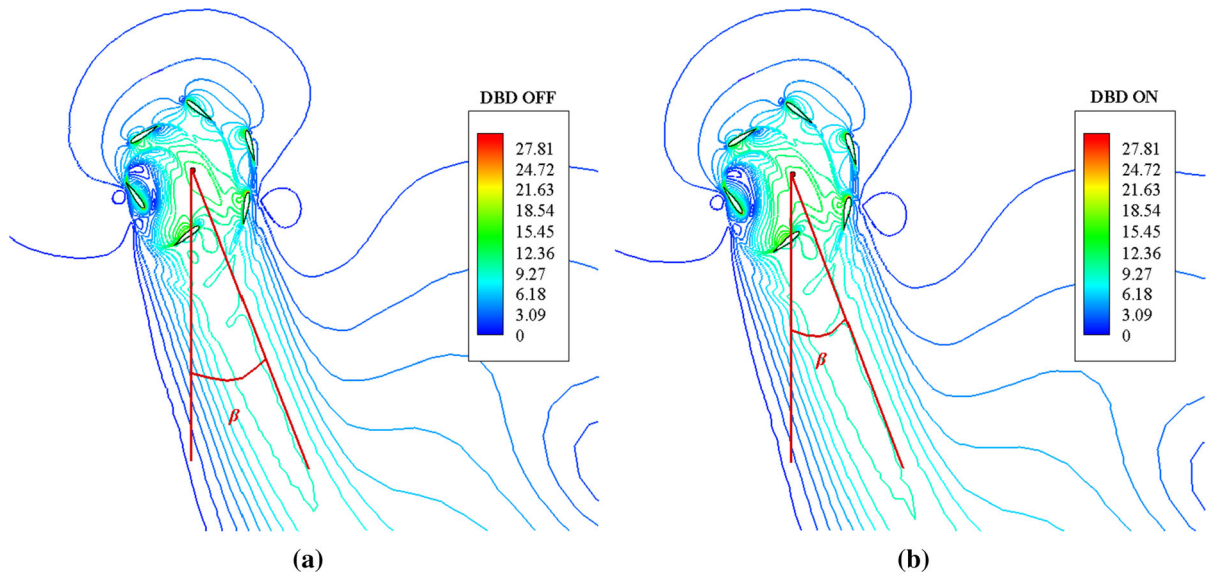


Fig. 21 Velocity magnitude contour plots: **a** actuation off, $\beta = 21.7^\circ$; **b** control actuation with six-DBDs, $\beta = 20.6^\circ$

$$DL = \frac{T_n}{A}, \tag{13}$$

The net thrust T_n and the power P_n are defined according to Eqs. (14) and (15) respectively:

$$T_n = \sqrt{T_H^2 + T_V^2}, \tag{14}$$

$$P_n = M \Omega, \tag{15}$$

M and A present the momentum and the projected frontal area of the cyclorotor respectively, Ω is the rotational speed; T_H and T_V are the horizontal and vertical thrusts.

we are able to compute the power consumption of the plasma actuator (P_p) based on a correlation of Jae-San Yoon and Jae-Hung Han [60] and Abdollahzadeh et al. [29], and that can be defined as follows:

$$\frac{P_p}{l_p} = 2\pi C_{eq}(U_0 - V_{bd})^2, \tag{16}$$

U_0 , V_{bd} and l_p are the applied voltage, breakdown voltage and the length of the plasma actuator that is considered in our DBD model, respectively.

C_{eq} is the equivalent capacitance of the plasma actuator, which is defined as:

$$C_{eq} = \frac{C_a C_b}{C_a + C_b}, \tag{17}$$

C_a and C_b present the equivalent capacitor properties between the electrodes, calculated as:

$$C_a = \frac{2\pi\epsilon_0}{\ln\left(\frac{0.5t_e + \lambda_d}{0.5t_e}\right)}, \tag{18}$$

$$C_b = \frac{\pi\epsilon_d}{\ln\left(\frac{0.5t_e + 2t_d}{0.5t_e}\right)}, \tag{19}$$

where $\epsilon_0 = 8.85 \times 10^{-19} \frac{E}{m}$, $\epsilon_r = 3$ and $\epsilon_d = \epsilon_0 \epsilon_r$. [29]

The Debye length is λ_d (mm) is computed from the relation provided in [60]:

$$\lambda_d = 0.2(0.3 \times 10^{-3} U_0(KV) - 7.42 \times 10^{-4}). \tag{20}$$

The different parameters used to define the DBD plasma actuator are obtained from experiments of Roth et al. [61] and Shyy et al. [27] are:

The electrode thickness is $t_e = 0.1$ mm, the dielectric thickness is $t_d = 0.75$ mm and the length of plasma is $l_p = 270$ mm. Finally, we obtain the power consumption of the actuator $P_p = 1.112$ W.

The control strategy used herein is for activating the actuators when they are going to be most effective, thus, in one cycle (0.3s) the actuators are activated in only 60° that corresponds to 0.05s, so the total energy consumption of the DBDs for a case with 6DBDs is:

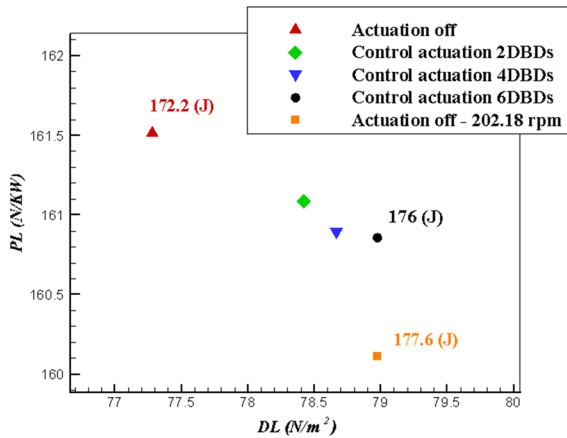


Fig. 22 Power loading variation with disk loading for base case and coupled cyclorotor with multi-DBD actuators

$$E_p = 1.112 \times n \times 0.05 = 2(J). \tag{21}$$

where n is number of actuators. The total energy of the cyclorotor with control actuation, with six-DBDs per cycle (0.3s) is:

$$E = E_c \times 0.3 + E_p = 176(J). \tag{22}$$

where E_c is the power consumption of the isolated cyclorotor system.

For the isolated cyclorotor at 202,18 rpm to achieve the same thrust $E_c = 177.6 (J)$.

From Fig. 22, it is clear that using six DBDs, three in each side of the blade is more effective and improved the thrust by 2.3% as compared to the base case, and achieving a reduction in power requirements of 0.9%, than increase the rotational speed to 202.1877 rpm to achieve the same thrust. This allows us to consider that even more gains may be achieved if the actuators are operated in duty cycle and employing an optimum position, or it may be a way to use thinner airfoils (less mass) and have the recirculation zone mitigated due to DBD plasma actuators.

In the current study, we showed that active flow control is an important element for the flow separation control around the blades. The results showed that the use of the proposed control law to activate the plasma actuators located on the upper and lower sides of the blades improves the lift and the thrust produced, which can play a key role for cycloidal rotor performance improvement. This effect of using plasma actuators with the proposed control law results in a counter-virtual camber effect in different azimuth positions,

due to the effective variation of the angle of attack along the chord as shown in Fig. 16. Which is seen as a negative camber equivalent at the top position, where the upper actuation is activated, and a positive camber equivalent at the bottom position, where the lower actuation is activated. This is reduced by the counter-virtual camber.

4 Conclusion

In this study we have performed a detailed analysis of the start-up characteristic of a cycloidal rotor from rest until reaching the nominal working point, namely the aerodynamic force, the vorticity and velocity contours. Then, we investigated the effect of using multiple plasma body forces on the flow field by using multi-DBD actuators on each blade of the cyclorotor. A CFD simulation was carried out using ANSYS FLUENT software, in which a user-defined function (UDF) was used to implement the cyclorotor movement and a second one to implement the plasma body force, the results show that:

- From the vorticity field, it was noticed that during the entire rotations, a periodic vortex shedding phenomenon was found, namely: flow attachment on the airfoil surface, flow separation from the leading edge then to the trailing edge, and flow reattachment to the airfoil surface. Also, it was noticed that in the upper half area the vortices on the upper section of the blade are more developed. When the blade rotates further in the lower half, the vortices are now generated on the bottom surface of the blade.
- From the velocity contour and the streamlines at the first time, starting from rest, inside the rotor cage there was a recirculation zone whose streamlines are closed and symmetrical with respect to the cyclorotor rotation in counter clockwise direction. As the blades rotate further, this zone moved with an inclination towards the right, before the flow starts entering in the rotor cage, while two circular vortex zones are created on the left and right sides of the cyclorotor. Due to rotation at different velocities, at the top and bottom positions, caused by the cyclorotor and the interactions of blades wakes, a downwash jet flow is generated, exiting

the bottom zone, which becomes stronger with rotation.

- We showed that active flow control with the use of the proposed control law, to switch between the upper and lower actuators, is an important element that helps to control and reduce the flow separation around the blades. This effect of using plasma actuators with the proposed control law results in a counter-virtual camber effect in different azimuth positions, due to the effective variation of the angle of attack along the chord. This effect is effective at the top position, where the upper actuation is activated, and at the bottom position, where the lower actuation is activated. Thus, it was advantageous to achieve more lift and thrust, as compared to the base case, in which the cyclorotor is now more stable in hover and vertical displacements.
- The use of multi-DBD actuators have more impact on the flow separation control and can modify instantaneously the flow around the blades. The configuration with six actuators, three in each side of the blade, was the most effective, by improving the thrust by 2.3%, as compared to the base case, and achieving a reduction in power requirements of 0.9%. Even though this reduction is not strong, it allows us to consider that even more gains may be achieved if the actuators are operated in duty cycle and employing an optimum position, or it may be a way to use thinner airfoils (less mass) and have the recirculation zone mitigated due to DBD plasma actuators.

Acknowledgements This work was supported by Project “EMaDeS –Energy, Materials and Sustainable Development No 01-0145-FEDER-000017, co-financed by the Portugal 2020 Program (PT2020), within the Regional Operational Program of the Center (CENTRO2020) and the European Union through the European Regional Development Fund (ERDF). This work was also supported by C-MAST, Center for Mechanical and Aerospace Science and Technology Research Unit No 151 within ClusterDEM lab at Universidade da Beira Interior. (Portugal).

Declarations

Conflict of interest The authors declare that they have no conflict of interest.

References

1. Yun CY, Park IK, Hwang IS, Kim SJ (2005) Thrust control mechanism of VTOL UAV cyclocopter with cycloidal blades system. *J Intell Mater Syst Struct* 16(11–12):937–943
2. McNabb M (2001) Development of a cycloidal propulsion computer model and comparison with experiment
3. Benedict M, Mataboni M, Chopra I, Masarati P (2010) Aeroelastic analysis of a MAV-scale cycloidal rotor. In: 51st AIAA/ASME/ASCE/AHS/ASC structures, structural dynamics, and materials conference 18th AIAA/ASME/AHS adaptive structures conference 12th, p 2888
4. Yong YC, Ilkyung P, Yong LH, Sang JJ, Seong HI, Jo KS, Nam JS (eds) (2004) A new VTOL UAV cyclocopter with cycloidal blades system. In: American Helicopter Society 60th Annual Forum, Baltimore. Citeseer
5. Jakson M, Pascoa JC, Xisto C (2013) Analytical modeling of a cyclorotor in forward flight. Technical report, SAE Technical Paper
6. Leger JA, Páscoa JC, Xisto CM (2015) Analytical modeling of a cyclorotor in hovering state. *Proc Inst Mech Eng Part G J Aerospace Eng* 229(12):2163–2177
7. Jiwei Tang YH, Song B, Yang H (2018) An unsteady free wake model for aerodynamic performance of cycloidal propellers. *Proc Inst Mech Eng Part G J Aerospace Eng* 232(2):290–307
8. Kim S, Yun C, Kim D, Yoon Y, Park I (2003) Design and performance tests of cycloidal propulsion systems. In: 44th AIAA/ASME/ASCE/AHS/ASC structures, structural dynamics, and materials conference, p 1786
9. Hu Y, Kah L, Hu W (2006) The research on the performance of cyclogyro, p 7704
10. Hwang IS, Min S, Lee CH, Kim S (2008) Development of a Four-Rotor Cyclocopter. *J Aircraft* 45(2151–2157):11
11. Nakaie Y, Ohta Y, Hishida K (2010) Flow measurement around a cycloidal propeller. *J Visual* 13:303–310
12. Benedict M, Jarugumilli T, Chopra I (2013) Effect of rotor geometry and blade kinematics on cycloidal rotor hover performance. *J Aircraft* 50:1340–1352
13. Benedict M, Jarugumilli T, Lakshminarayan V, Chopra I (2014) Effect of flow curvature on forward flight performance of a micro-air-vehicle-scale cycloidal-rotor. *AIAA J* 52(6):1159–1169
14. Monteiro JAL, Páscoa J (2018) Effects of harmonic vibration on cycloidal rotor performance. In: ASME international mechanical engineering congress and exposition, vol 52002. American Society of Mechanical Engineers, p V001T03A003
15. Leger J, Páscoa J, Xisto C (2015) 3D effects in cyclorotor propulsion systems. In: ASME international mechanical engineering congress and exposition, vol 57342. American Society of Mechanical Engineers, p V001T01A004
16. Xisto CM, Páscoa JC, Abdollahzadeh M, Leger JA, Schwaiger M, Wills D, Masarati P, Gagon L (2014) PECyT-plasma enhanced cycloidal thruster. In: 50th AIAA/ASME/SAE/ASEE joint propulsion conference, p 3854
17. Xisto CM, Leger JA, Páscoa JC, Gagnon L, Masarati P, Angeli D, Dumas A (2017) Parametric analysis of a large-

- scale cycloidal rotor in hovering conditions. *J Aerospace Eng* 30(1):04016066
18. Habibnia M, Pascoa J (2019) ANN assisted flow modeling and analysis for a cyclorotor in ground effect. *Aerosp Sci Technol* 95:105495
 19. Yu H, Chang T, Lang ZH (2014) An investigation into the effect of the airfoil on the aerodynamics of the MAV scale cycloidal propeller under hovering status. In: *AIAA AVIATION 2014–14th AIAA Aviation Technology, Integration, and Operations Conference* 01
 20. Hu Y, Fu X, Zhang H, Wang G, Farhat H (2019) Effects of blade aspect ratio and taper ratio on hovering performance of cycloidal rotor with large blade pitching amplitude. *Chin J Aeronaut* 32(5):1121–1135
 21. Stasko T, Dykas S, Majkut M, Smolka K et al (2019) An attempt to evaluate the cycloidal rotor fan performance. *Open J Fluid Dyn* 9(04):292
 22. Gagnon L, Morandini M, Quaranta G, Masarati P, Xisto CM, Páscoa JC (2018) Aeroelastic analysis of a cycloidal rotor under various operating conditions. *J Aircraft* 55(4):1675–1688
 23. McElreath JW, Benedict M, Tichenor N (2020) Cycloidal rotor-blade tip-vortex analysis at low Reynolds number. *AIAA J* 58(6):2560–2570
 24. Rodrigues F, Mushyam A, Pascoa J, Trancossi M (2019) A new plasma actuator configuration for improved efficiency: the stair-shaped dielectric barrier discharge actuator. *J Phys D Appl Phys* 52(38):385201
 25. Abdollahzadeh M, Rodrigues F, Pascoa JC, Oliveira PJ (2015) Numerical design and analysis of a multi-DBD actuator configuration for the experimental testing of Acheon nozzle model. *Aerosp Sci Technol* 41:259–273
 26. West T, Hosder S (2012) Numerical investigation of plasma actuator configurations for flow separation control at multiple angles of attack. In: *6th AIAA flow control conference*, p 3053
 27. Shyy W, Jayaraman B, Andersson A (2002) Modeling of glow discharge-induced fluid dynamics. *J Appl Phys* 92(11):6434–6443
 28. Massines F, Rabehi A, Decomps P, Gadri RB, Ségur P, Mayoux C (1998) Experimental and theoretical study of a glow discharge at atmospheric pressure controlled by dielectric barrier. *J Appl Phys* 83(6):2950–2957
 29. Abdollahzadeh M, Pascoa JC, Oliveira PJ (2014) Modified split-potential model for modeling the effect of DBD plasma actuators in high altitude flow control. *Curr Appl Phys* 14(8):1160–1170
 30. Abdollahzadeh M, Pascoa JC, Oliveira PJ (2018) Comparison of DBD plasma actuators flow control authority in different modes of actuation. *Aerosp Sci Technol* 78:183–196
 31. Suzen Y, Huang G, Jacob J, Ashpis D (2005) Numerical simulations of plasma based flow control applications. In: *35th AIAA fluid dynamics conference and exhibit*, p 4633
 32. Jayaraman B, Shyy W (2003) Flow control and thermal management using dielectric glow discharge concepts. In: *33rd AIAA fluid dynamics conference and exhibit*, p 3712
 33. Visbal M, Gaitonde D, Roy S (2006) Control of transitional and turbulent flows using plasma-based actuators. In: *36th AIAA fluid dynamics conference and exhibit*, p 3230
 34. Orlov D, Apker T, He C, Othman H, Corke T (2007) Modeling and experiment of leading edge separation control using SDBD plasma actuators. In: *45th AIAA aerospace sciences meeting and exhibit*, p 877
 35. He C, Corke T, Patel M (2007) Numerical and experimental analysis of plasma flow control over a hump model. In: *45th AIAA aerospace sciences meeting and exhibit*, p 935
 36. Rizzetta DP, Visbal MR (2008) Plasma-based flow-control strategies for transitional highly loaded low-pressure turbines. *J Fluids Eng* 130(4):041104
 37. Giorgi MGD, Motta V, Suma A (2020) Influence of actuation parameters of multi-DBD plasma actuators on the static and dynamic behaviour of an airfoil in unsteady flow. *Aerosp Sci Technol* 96:105587
 38. Zhang PF, Liu AB, Wang JJ (2010) Flow structures in flat plate boundary layer induced by pulsed plasma actuator. *SCIENCE CHINA Technol Sci* 53(10):2772–2782
 39. Cho Y-C, Shyy W (2011) Adaptive flow control of low-Reynolds number aerodynamics using dielectric barrier discharge actuator. *Prog Aerosp Sci* 47(7):495–521
 40. Riherd P, Roy S, Visbal M (2011) Numerical investigation of serpentine plasma actuators for separation control at low Reynolds number. In: *41st AIAA fluid dynamics conference and exhibit*, p 3990
 41. Khoshkhoo R, Jahangirian A (2016) Flow separation control over airfoils using DBD plasma body force. *J Braz Soc Mech Sci Eng* 38(8):2345–2357
 42. Borghi CA, Cristofolini A, Neretti G, Seri P, Rossetti A, Talamelli A (2017) Duty cycle and directional jet effects of a plasma actuator on the flow control around a naca0015 airfoil. *Meccanica* 52(15):3661–3674
 43. Javadi K, Hajipour M (2017) Separation control using quasi-radial wall jets. *Aerosp Sci Technol* 68:240–251
 44. Ebrahimi A, Hajipour M (2018) Flow separation control over an airfoil using dual excitation of DBD plasma actuators. *Aerosp Sci Technol* 79:658–668
 45. Akbarzadeh P, Askari Lehdarbonei A, Derazgisoo SM (2018) Low reynolds unsteady flow simulation around naca0012 airfoil with active flow control. *Meccanica* 53(14):3457–3476
 46. Megawanto FC, Budiarmo H, James J (2018) Numerical analysis of plasma actuator for drag reduction and lift enhancement on NACA 4415 airfoil. *AIP Publishing LLC*, p 050001
 47. Ben-Harav A, Greenblatt D (2016) Plasma-based feed-forward dynamic stall control on a vertical axis wind turbine. *Wind Energy* 19(1):3–16
 48. Ma L, Wang X, Zhu J, Kang S (2019) Dynamic stall of a vertical-axis wind turbine and its control using plasma actuation. *Energies* 12(19):3738
 49. Omidi J, Mazaheri K (2020) Wind turbine generated power enhancement by plasma actuator. *arXiv preprint arXiv:2004.07046*
 50. Worasinchai S, Ingram GL, Dominy RG (2012) The physics of h-darrieus turbines self-starting capability: flapping-wing perspective. *Turbo Expo: Power for Land, Sea, and Air*, vol 44724. American Society of Mechanical Engineers, pp 869–878
 51. Biadgo MA, Simonović A, Komarov D, Stupar S (2013) Numerical and analytical investigation of vertical axis wind turbine. *FME Trans* 41(1):49–58

52. Zhu J, Huang H, Shen H (2015) Self-starting aerodynamics analysis of vertical axis wind turbine. *Adv Mech Eng* 7(12):1687814015620968
53. Tang J, Hu Y, Song B (2015) Investigation on the unsteady aerodynamics of cycloidal propeller in hovering flight. *Proc Inst Mech Eng Part G J Aerospace Eng* 229(13):2519–2536
54. Abdelraouf H, Elmekawy AMN, Kassab SZ (2020) Simulations of flow separation control numerically using different plasma actuator models. *Alex Eng J* 59(5):3881–3896
55. Yu H, Zheng J (2020) Numerical investigation of control of dynamic stall over a naca0015 airfoil using dielectric barrier discharge plasma actuators. *Phys Fluids* 32(3):035103
56. Benmoussa A, Páscoa JC (2021) Cycloidal rotor coupled with DBD plasma actuators for performance improvement. *Aerospace Sci Technol* 110:106468
57. Singh K, Páscoa JC (2018) Numerical modeling of stall and poststall events of a single pitching blade of a cycloidal rotor. *J Fluids Eng* 141(1):011103
58. Rezaeiha A, Montazeri H, Blocken B (2019) On the accuracy of turbulence models for CFD simulations of vertical axis wind turbines. *Energy* 180:838–857
59. Wills D, Schwaiger M (2012) In USEUCOM. Science & Technology Conference
60. Yoon J-S, Han J-H (2015) Semiempirical thrust model of dielectric barrier plasma actuator for flow control. *J Aerosp Eng* 28(1):04014041
61. Roth JR, Sherman DM, Wilkinson SP (2000) Electrohydrodynamic flow control with a glow-discharge surface plasma. *AIAA J* 38(7):1166–1172

Publisher's Note Springer Nature remains neutral with regard to jurisdictional claims in published maps and institutional affiliations.